
Neutron Yield Study of Direct-Drive, Low-Adiabatic Cryogenic D₂ Implosions on OMEGA

Introduction

As a viable path to energy production, inertial confinement fusion (ICF) has been actively pursued over the past decades.¹ In a standard ICF design, a thin-shell capsule containing a solid DT (ice) layer and low-density DT gases is imploded as symmetrically as possible, either directly driven by high-energy lasers² or indirectly driven by x rays in a hohlraum.³ The high-speed, inward-moving shell compresses the low-density DT gases, thereby creating a “hot spot” during the stagnation of the implosion. Thermonuclear reactions in this high-temperature hot spot can trigger a burn wave that ignites the assembled, surrounding high-density fuel. To obtain energy gain, the imploding DT fuel must be compressed to thousands of times its solid density.⁴ On one hand, a properly created hot spot, with certain density and temperature, provides the alpha (α) particles for subsequent heating of the assembled, surrounding high-density, low-temperature fuels. On the other hand, the fuel areal density (ρR) must be high enough to stop the heating particles for efficient burn-wave propagation. It is clear that proper hot-spot formation and high-density fuel assembly must be attained simultaneously to guarantee a successful ignition. Any target perturbations can grow exponentially via Rayleigh–Taylor (RT) instability^{5–9} to disrupt the hot-spot formation as well as the high-density fuel assembly.

Cryogenic implosions with high adiabats of $\alpha \geq 4$ (α is defined as the ratio of fuel pressure to the Fermi-degenerate pressure) have been previously investigated in OMEGA experiments¹⁰ and simulations.¹¹ To efficiently compress ICF targets to high densities, the fuel must maintain a low adiabat of $\alpha \simeq 2$ during a direct-drive implosion.¹² Low-adiabat implosions are very sensitive, however, to RT instability growth. Mitigation of RT growth has been proposed and conducted using a laser picket in front of the main pulse, which shapes the fuel adiabat to be low at the back surface and high at the ablation front.^{13,14} A series of such shaped low-adiabat ($\alpha \simeq 2$ to 3) cryogenic targets have been imploded at the OMEGA Laser Facility.^{15–17} Since efficient diagnostic methods for ρR measurement of DT implosions are not yet fully implemented, most cryogenic implosions on OMEGA are currently performed

with D₂ targets. For D₂ implosions, the compression has been successfully measured up to $\rho R \sim 200$ mg/cm² by secondary proton scattering.^{15–17} As discussed above, assembly of high-density fuels is extremely crucial, but getting the predicted fusion yield from the formed hot spot is equally important to the success of ICF; after all, it provides the “trigger” for ignition burn propagation to occur. A variety of perturbations can significantly reduce the fusion yield. This article is devoted to understanding the perturbation sources and how they affect the neutron yield in low-adiabat cryogenic D₂ implosions conducted on OMEGA.

The next two sections give a brief description of the two-dimensional (2-D) numerical simulations and experimental basics, respectively. Subsequent sections (1) present simulation results that examine in detail the effects of both individual and combined perturbation sources on the implosion yield degradation; (2) discuss the absolute experimental neutron yield and neutron rate measurements, when compared to our modelings; and (3) summarize our results.

Two-Dimensional DRACO Simulations

The 2-D radiation hydrodynamics code *DRACO* has been developed at LLE for both implosion and planar target simulations.¹⁸ *DRACO* can be run in either Lagrangian, Eulerian, or Arbitrary–Lagrangian–Eulerian (ALE) mode, but this study uses only the ALE version. For spherical implosion simulations, the *DRACO* coordinates are defined by the cylindrical axis z and radius R , with the assumption of azimuthal symmetry. The laser absorption of plasmas through inverse bremsstrahlung is implemented by three-dimensional (3-D) ray tracing with the exact port geometry of OMEGA.¹⁹ Although *DRACO* has the option of using different equations of state (EOS’s) in hydro-simulations, the *SESAME* EOS table²⁰ is used throughout this study. The *SESAME* EOS of direct-drive ICF shell material has recently been verified by compressibility measurements.^{21,22} Agreements were found for a variety of drive conditions related to direct-drive ICF. The radiation transport in *DRACO* has used the multigroup diffusion model, in which the Astrophysics Opacity Table (AOT)²³ is applied.

Since the laser energy absorbed near the critical-density region must be transported to the ablation surface by electrons, the thermal-transport model in direct-drive ICF is crucial for properly simulating the target drive. There has been a long history of using flux-limited Spitzer thermal conductivity in laser-plasma fluid modelings.²⁴ Previous experiments with both planar and spherical targets^{25,26} have shown that a flux limiter of $f = 0.06$ works well for low/middle laser intensities (up to $\sim 6 \times 10^{14}$ W/cm²) of square pulses; however, there was also evidence that a time-dependent flux limiter²⁷ or a nonlocal heat-transport model¹⁶ is required to better simulate implosions driven by high-intensity lasers and/or sophisticated pulse shapes. In principle, we can perform our 2-D simulations with a time-dependent flux limiter, which partially accounts for the nonlocal effects. However, since the purpose of this study is to explore the perturbation effects on the neutron-yield degradation of implosions, we have confined our simulations to those shots that are insensitive to the heat-transport model. Namely, we have studied mostly cryogenic D₂ implosions with low/middle laser intensities ranging from 2.5 to 6×10^{14} W/cm². For those implosions, the local and nonlocal 1-D LILAC²⁸ simulations show less sensitivity to shock timing; therefore, a normal flux limiter of $f = 0.06$ was adopted for these studies.

DRACO’s capability to simulate Rayleigh–Taylor instability growth has recently been demonstrated with intense laser-driving planar-target experiments on OMEGA.²⁹ For low-mode perturbations similar to those investigated here, the code properly predicts their growth rate at the relevant laser-intensity range. Generally, we have examined an ice-layer roughness mode up to $\ell = 12$. The higher modes of ice-layer perturbations are found to be less important to yield degradation in thin-shell (~ 5 - μm) implosions.

D₂ Implosion Experiments on OMEGA

The 60-beam OMEGA Laser Facility delivers up to 30-kJ, 351-nm UV energies on target.³⁰ A typical laser pulse used for low-adiabat D₂ implosions is shown in Fig. 116.7(b), in which the Gaussian-like laser picket is used to shape the target adiabat.^{13,14} Each laser beam, coming from ports in 3-D geometry, is equipped with an SG-4 phase plate. Standard beam-smoothing techniques were used, including distributed phase plates,³¹ polarization smoothing,³² and smoothing by spectral dispersion (SSD).³³ The power imbalance (PI) among beams has an rms (root mean square) of $\sim 2.6\%$, while the mistiming (MT) is typically within ~ 12 -ps rms. The mistiming of each beam has an uncertainty of ~ 12 - μm rms. All of these low-mode laser nonuniformities have been implemented in our 3-D ray-tracing laser-absorption package. We have separately

examined the effect of each of these nonuniformities and their combined effects on the performance of a uniform target. The simulation results are summarized in Table 116.I. Compared to the uniform irradiation, it was found that mistiming among beams is the dominant effect to the total yield-over-clean (YOC) degradation, while other low-mode laser perturbations change the YOC only a few percent around that of the symmetric implosion. The “clean” yield is defined as the neutron yield from a 2-D simulation with uniform laser irradiation and

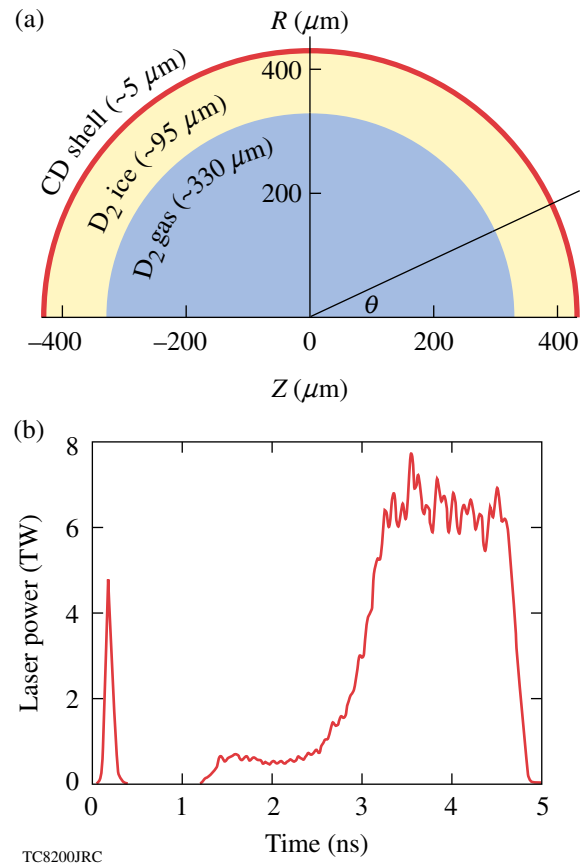


Figure 116.7 (a) The schematic diagram of a typical thin-shell cryogenic D₂ target imploded on OMEGA; (b) the shaped low-adiabat ($\alpha \simeq 2$ to 3) laser pulse with a picket.

Table 116.I: YOC dependence on low-mode laser nonuniformities.

Low-mode laser nonuniformity	YOC _{2-D}
3-D port geometry only	96.7%
Geometry + mispointing ($\sim 12 \mu\text{m}$)	98.0%
Geometry + power imbalance ($\sim 2.6\%$)	102%
Geometry + mistiming (~ 12 ps)	82.2%
Full nonuniformity (including all)	83.3%

a symmetric target. It shows that all of these combined illumination nonuniformities reduce the YOC to a level of ~83% for a uniform target. All of the following studies have included these low- ℓ -mode laser nonuniformities since they are always present in OMEGA experiments.

Detailed descriptions of cryogenic targets formed for OMEGA implosions can be found in Refs. 34 and 35. Basically, the targets are D₂ filled, with a CD shell having an outer diameter of ~860 μm and a shell thickness of 5 to 10 μm . The targets are permeation filled with high-pressure D₂ gas and cooled to below the triple point (~18.7 K). They are then transported to a characterization station for layer formation and finally to the OMEGA target chamber for implosion. The ice-layer roughness is measured in experiment before implosion. The actual low-mode spectrum of ice roughness is used in our simulations.

A typical target [shown schematically in Fig. 116.7(a)] has an ice layer of ~95- μm thickness. Figure 116.8 illustrates the irradiation nonuniformity in the case of non-zero target offset. The target offset is caused by oscillation when the shroud is pulled before implosion. This initial target offset is measured through an x-ray pinhole camera image at the beginning of corona plasma formation.¹⁰ The fusion yield is measured by a combination of activation, scintillation, and track recorder. When compared to the predicted symmetric implosion yield, the YOC provides a direct measurement of target performance.

The low-adiabat cryogenic implosion campaign conducted on OMEGA used a wide range of peak laser intensities up to $\sim 10^{15}$ W/cm². For high intensities near $\sim 10^{15}$ W/cm², the compression is somewhat degraded with respect to the standard 1-D prediction due to different mechanisms.^{15,16,36} Thus, this study of neutron-yield degradation will focus on those low- to mid-intensity shots that obtained $\langle \rho R \rangle_{\text{exp}}$ better than 60% of the standard 1-D prediction. They are generally in the range of $\langle \rho R \rangle_{\text{exp}} \simeq 100$ to 200 mg/cm².

Results and Discussions

Using the laser pulse shown in Fig. 116.7(b) throughout this general study, we will first address, separately, the effects induced by pure offset and pure ice roughness on the YOC degradation. We then discuss their combined effects on reducing the neutron yield. Finally, we compare the simulation results to experiments. The absolute neutron yields and rates from DRACO simulations are also compared with measurements for individual shots. Note that the laser nonuniformities discussed above have been included in all of the following studies since they are always present in OMEGA experiments.

1. Pure Offset

For the target and pulse shape characterized in Fig. 116.7, we simulated implosions with different initial target offsets but no ice roughness present (symmetric target). The offset is along the positive z axis, thereby leading to more irradiation on the “left” side than on the “right” side of the target. This can be

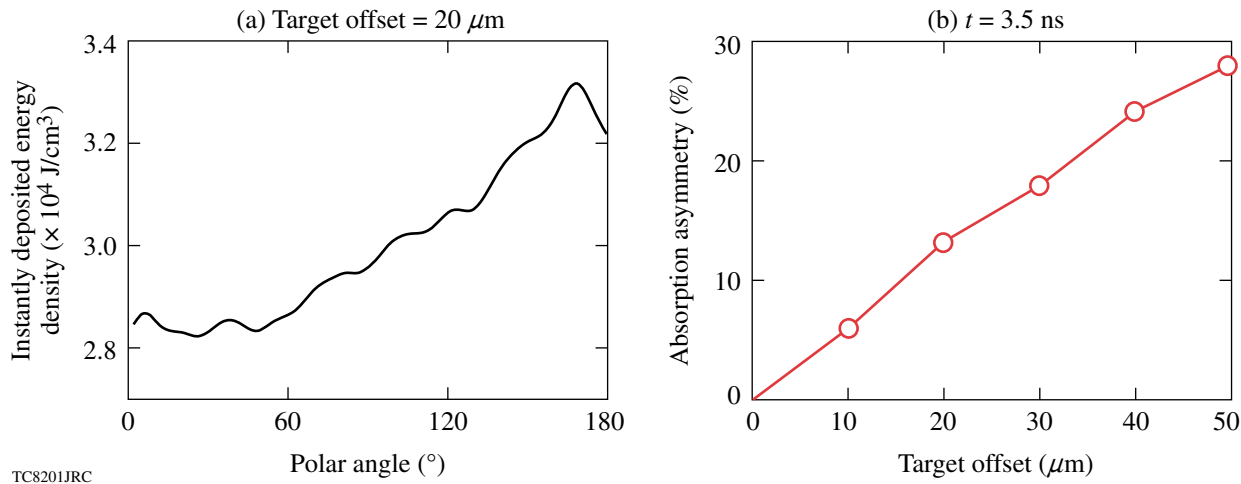


Figure 116.8 (a) The deposited energy density at $t = 3.5 \text{ ns}$ versus the angle θ (relative to the $+z$ axis) for a target offset of $20 \mu\text{m}$; (b) the absorption asymmetry plotted as a function of target offset.

seen in Fig. 116.8(a) for the case of a 20- μm offset, in which is plotted the instantly absorbed laser energy density (ED) at time $t = 3.5$ ns as a function of the polar angle θ [defined in Fig. 116.7(a)]. The $\theta = 0^\circ$ line is along the positive z axis, while $\theta = 180^\circ$ is for the negative z axis. The absorption asymmetry is defined as

$$\text{absorption symmetry} = \frac{\text{ED}_{\max} - \text{ED}_{\min}}{\text{ED}_{\text{avg}}}, \quad (1)$$

where ED_{\max} , ED_{\min} , and ED_{avg} are the temporal maximum, minimum, and averaged energy-density depositions in the full range of polar angle θ . For the case of zero offset, the symmetric illumination gives no absorption asymmetry, while it reaches to $\sim 13\%$ at a 20- μm offset. In Fig. 116.8(b), the absorption asymmetry is plotted at $t = 3.5$ ns as a function of the initial target offset. Approximately 30% more laser absorption is seen on the left side than on the right side of the target in the case of a 50- μm offset. The uneven drive compresses the target asymmetrically, thereby reducing the final hot-spot temperature and density, which leads to neutron-yield degradation. As examples, the density contours are plotted at the peak compression time ($t = 4.9$ ns) for the cases of 20- μm and 40- μm offset in Figs. 116.9(a) and 116.9(b) and the neutron rates as a function of time in Fig. 116.9(c). It can be seen that the larger the offset, the more asymmetric the compression. Consequently, the hot-spot ion temperature and density decrease from $T_i \simeq 1.8$ keV and $\rho \simeq 9$ g/cm³ to $T_i \simeq 1.5$ keV and $\rho \simeq 7$ g/cm³ as the target offset increases from 20 μm [Fig. 116.9(a)] to 40 μm [Fig. 116.9(b)]. Compared to the symmetric case, a non-zero target offset has caused the ‘‘burn’’ to truncate early and has resulted in a relatively lower peak rate, thereby leading to an overall reduction in neutron yield, as shown in Fig. 116.9(c). The resulting $\text{YOC}_{2\text{-D}}$ decreases from 43% to 13.8% for these two cases, respectively.

Figure 116.10 explores the detailed hydrodynamics of how the offset affects hot-spot formation. Density snapshots at different times of (a) $t = 4.55$ ns, (b) $t = 4.65$ ns, (c) $t = 4.75$ ns, and (d) $t = 4.85$ ns are shown during shell stagnation for the case of 20- μm offset. Since the absorption on the target’s left side is constantly higher, the shock from the left side is stronger than that from the right side. The asymmetric shock converges and shifts to the right side, away from the core center. At $t = 4.55$ ns, the asymmetrically converged shock starts to bounce back. As evidence of the bounced shock asymmetry, the unevenly formed high-pressure region on the inner surface of the right side of the target is indicated by Fig. 116.10(b). This asymmetrically bounced shock acting with a continuously uneven drive makes the target convergence unequal from both sides.

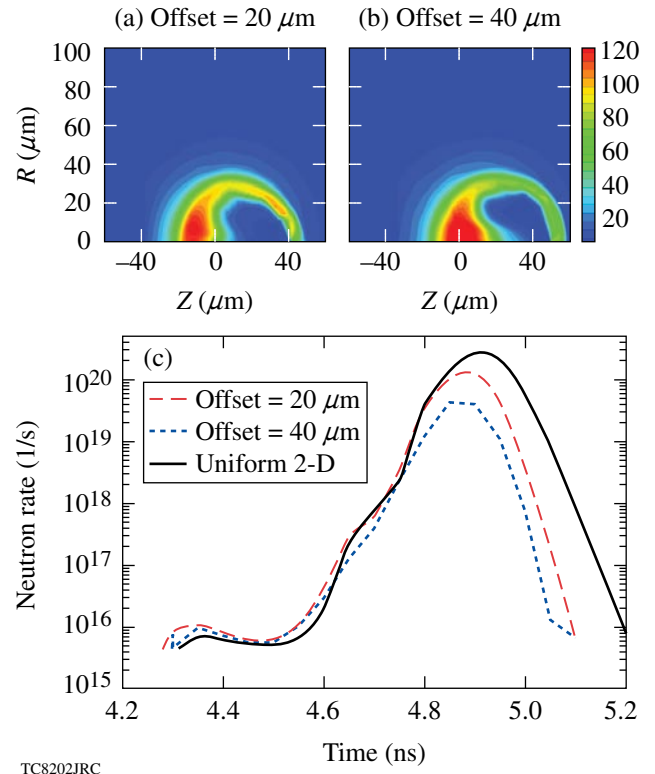


Figure 116.9
The density contour plots at peak compression for target offset of (a) 20 μm and (b) 40 μm . The corresponding neutron rates are plotted in (c) for the two offset situations as well as the symmetric case.

As time goes on, convergence is stronger on the left side of the target (opposite to the initial target offset direction), thereby leading to high compression along that side. All these features are presented in the simulations in Fig. 116.10.

Pure-offset simulations up to 50 μm have been performed with the pulse shape and uniform target characterized in Fig. 116.7; the results are summarized in Fig. 116.11. It is noted that at zero offset the laser illumination nonuniformities degrade the $\text{YOC}_{2\text{-D}}$ to $\sim 83\%$, as was addressed above. Overall, the $\text{YOC}_{2\text{-D}}$ monotonically decreases as the offset increases. For a target offset of 20 μm , the simulation gives a $\text{YOC} \sim 40\%$, which is three to four times higher than experimental observations. Thus, the target offset alone cannot explain the YOC degradation in experiments.

2. Ice Roughness Only

The ice-layer roughness has been characterized in experiments.³⁴ As an example, the low- ℓ -mode spectrum of ice roughness for a typical cryogenic D₂ target is shown in Fig. 116.12, with $\sigma_{\text{rms}} \simeq 3.2$ μm . Approximating the ice-layer

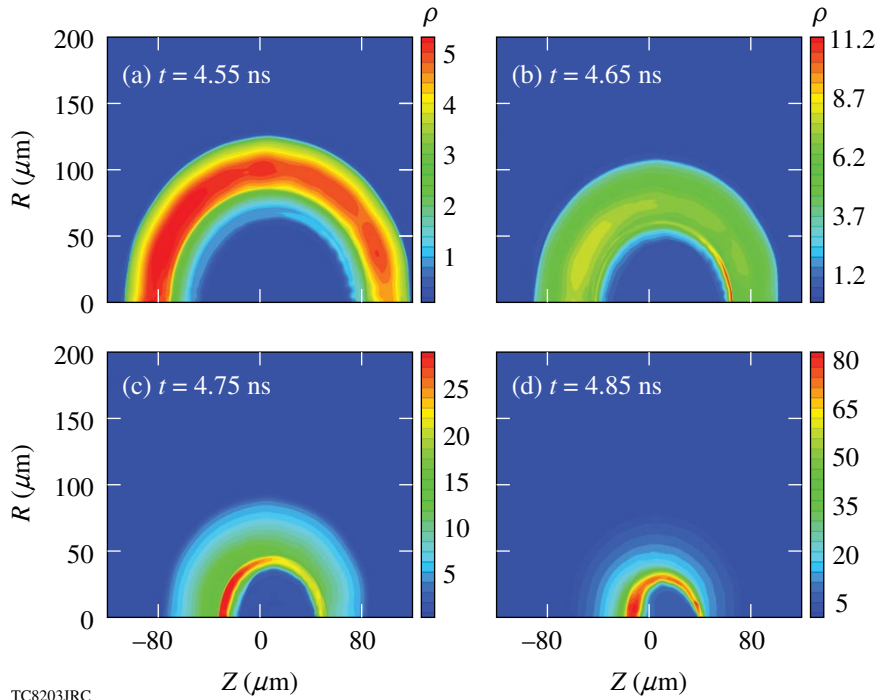
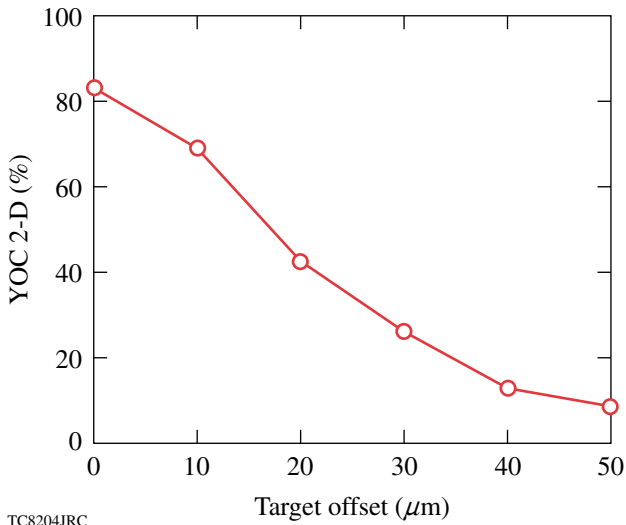


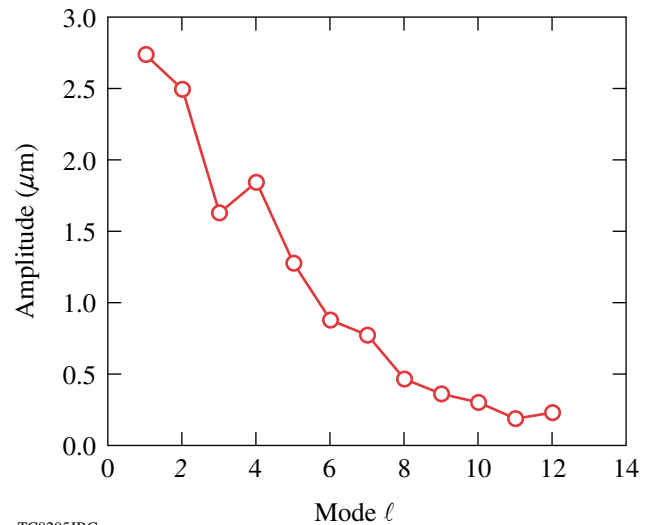
Figure 116.10
The density contour plots of a uniform target implosion with 20- μm offset, during the deceleration phase at times (a) $t = 4.55$ ns, (b) $t = 4.65$ ns, (c) $t = 4.75$ ns, and (d) $t = 4.85$ ns.

TC8203JRC



TC8204JRC

Figure 116.11
The $\text{YOC}_{2\text{-D}}$ as a function of target offset only.



TC8205JRC

Figure 116.12
The low- ℓ -mode spectrum of ice-layer roughness for a typical cryogenic D₂ target imploded on OMEGA.

perturbation as a sum of *cosine* modes, we construct the ice-layer thickness (ΔR) for our *DRACO* simulations. Namely,

$$\Delta R(\theta) = \Delta R_0 + \sum_{\ell=1}^n \pm A_{\ell} \cos(\ell\theta), \quad (2)$$

where ΔR_0 is the average thickness of the ice layer and A_{ℓ} is the perturbation amplitude of the ℓ th mode. Due to the

hydro-boundary conditions imposed in *DRACO*, the phase among different modes can only be either 0 or π radian. This gives a plus (+) or minus (−) sign in the superposition of each mode. Different combinations of these signs provide various phases of the ice layer, which give different perturbed shell thicknesses along the polar angle θ . For instance, three such phases are drawn in Fig. 116.13. We mark the shell thickness at

$\theta = 0^\circ$, $\theta = 90^\circ$, and $\theta = 180^\circ$ for each target condition. For the phase-1 target shown in Fig. 116.13(a), the thinnest ice layer is along the $\theta = 0^\circ$ axis, while the thickest portion is at $\theta = 90^\circ$. Figures 116.13(b) and 116.13(c) indicate the other two cases, of which the thinnest ice layer is along $\theta = 90^\circ$, but different conditions are indicated along the z axis.

Without target offset, simulations were performed for these three target conditions characterized in Fig. 116.13. The simulated results are presented in Figs. 116.14(a)–116.14(c) for density contours at peak compression and in Fig. 116.14(d) for neutron rates. Depending on which part is the thinnest ice layer, the shock will first break out there. For example, the shock breaks out early from the right side ($\Delta R = 90 \mu\text{m}$ at $\theta = 0^\circ$) of the target in the phase-1 condition. The asymmetrically converged shock will push the core toward the left side (along

the $\theta = 180^\circ$ direction). For targets in phases 2 and 3, the thinnest ice layer is along the $\theta = 90^\circ$ direction. When the shock breaks out early from there, it makes the final hot spot more elongated along the z axis as illustrated in Figs. 116.14(b) and 116.14(c). Consequently, we observe that the compressed core of the phase-1 target shifts to $z \simeq -10 \mu\text{m}$ at stagnation, while the center of mass moves roughly to $z \simeq +10 \mu\text{m}$ for phases 2 and 3. The phase-1 target gives a better performance than the other two targets. The $\text{YOC}_{2\text{-D}}$ is about 31% on average and varies within $\sim 3\%$ for these three phases. The yield performance is not sensitive to different phases in the case of zero offset, but this observation can be largely changed when combined to nonzero target offset. Even though an ice roughness of $\sigma \simeq 3.2 \mu\text{m}$ could significantly reduce the $\text{YOC}_{2\text{-D}}$ to a level of $\sim 30\%$, these simulations indicate that the ice roughness alone cannot explain the experimental YOC measurements. They are generally two to

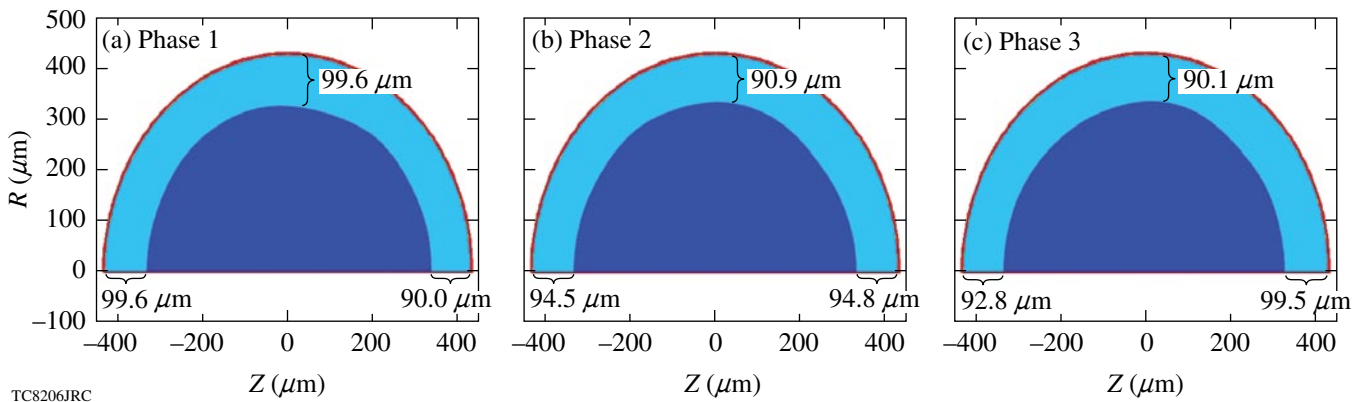


Figure 116.13
Different target conditions depending on the phases among low modes of the ice-layer roughness.

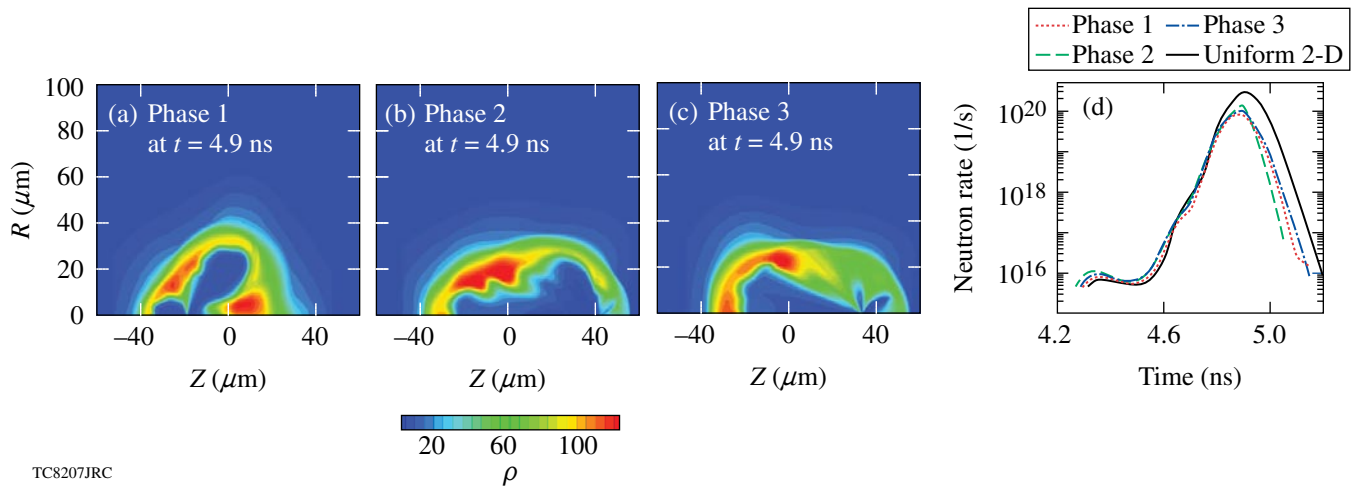


Figure 116.14
The density plots at peak neutron production, respectively, for the three different target conditions [(a), (b), and (c)] in Fig. 116.13. The corresponding neutron rates are shown in (d).

three times higher than the experimental YOC measurements, which have both ice roughness and nonzero target offset.

3. Combination of Target Offset and Ice Roughness

From here on, we examine the combined perturbation effects of both the target offset and the ice-layer roughness on the neutron-yield degradation of D₂ target implosions. Numerical examples are shown in Fig. 116.15 in the case of a 30- μm offset for the target ice-layer conditions illustrated in Fig. 116.13. In these figures, the density contours are plotted at the time of their peak neutron production. Overall, the offset acts like a dominant $\ell = 1$ mode that compresses the shell more on the left side (e.g., along the “anti-offset” direction). However, the detailed core configurations vary significantly for different phases of ice roughness. As seen in Fig. 116.14(a), the pure ice roughness in phase 1 gives a final compressed core shifted to $Z = -10 \mu\text{m}$, referred to here as the “equivalent offset” to the ice roughness. This equivalent offset is opposite the real target offset, which is set along the positive z direction. Namely, the two perturbation effects are “out of phase” as the hard-driven side (along $\theta = 180^\circ$) encounters a thicker ice layer [see Fig. 116.13(a)], so that the shocks breaking out from both sides are somewhat more balanced in phase 1. Thus, when combining the real target offset of $z = +30 \mu\text{m}$ with the phase-1 ice roughness, the final compressed core moves roughly to $z \simeq +30 - 10 \simeq 20 \mu\text{m}$ as indicated by Fig. 116.15(a). It therefore gives a better performance and results in more neutron production, shown as the thick, solid curve in Fig. 116.15(d). While for phases 2 and 3, the ice-roughness effect is “in phase” with the target offset perturbation. In other words, both perturbations constructively cause the target to perform less satisfactorily. Figures 116.15(b) and

116.15(c) show that the final cores shift to distances larger than their initial target offset of 30 μm ; therefore, both cases perform less satisfactorily than the phase-1 target. With the extra perturbation of offset, the target performance is now more sensitive to the phase of ice roughness. The final target performance actually depends on whether the target offset is in phase or out of phase with the ice roughness. We have also explored other phases and found that phases 1 and 2 shown here are the two extremes.

To characterize the hot-spot condition, the quantity of $\rho^2 T_i^4$ is plotted in Fig. 116.16 for the three cases shown in Fig. 116.15, where ρ and T_i are the D₂ density and the ion temperature, respectively. Since the fusion rate is proportional to this quantity,¹ these plots indicate where neutrons are probably generated and what portion of the core volume contributes to neutron production during peak compression. Bearing in mind the azimuthal symmetry imposed in DRACO, one can see from Fig. 116.16 that the core condition of the phase-1 target is much better (having more volume with higher $\rho^2 T_i^4$) than the other two cases, which is consistent with the higher neutron production from the phase-1 target.

By varying the target offset and the ice roughness, the effects of different combinations of the two on the implosion neutron yield have been numerically examined. The results are summarized in Fig. 116.17, which plots the YOC_{2-D} versus the initial target offset for ice roughnesses of $\sigma_{\text{rms}} = 1.0 \mu\text{m}$ and $\sigma_{\text{rms}} = 3.2 \mu\text{m}$. All phases explored for each point have been averaged; also indicated is the YOC_{2-D} range that each target phase could possibly reach. Figure 116.17 shows that, as the

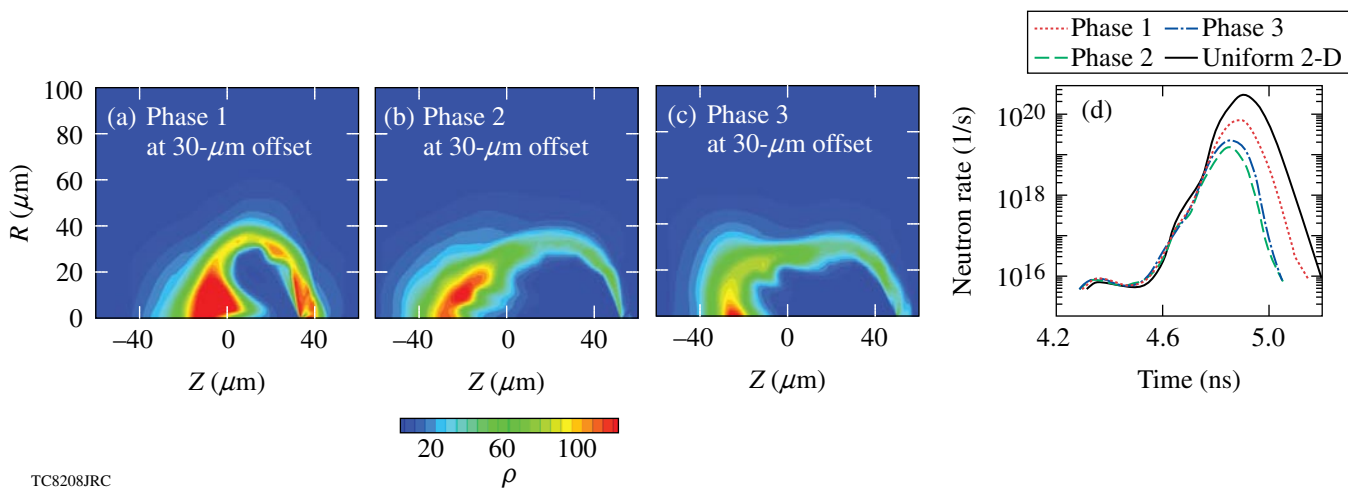


Figure 116.15
Similar to Fig. 116.14, but the targets are now offset by 30 μm .

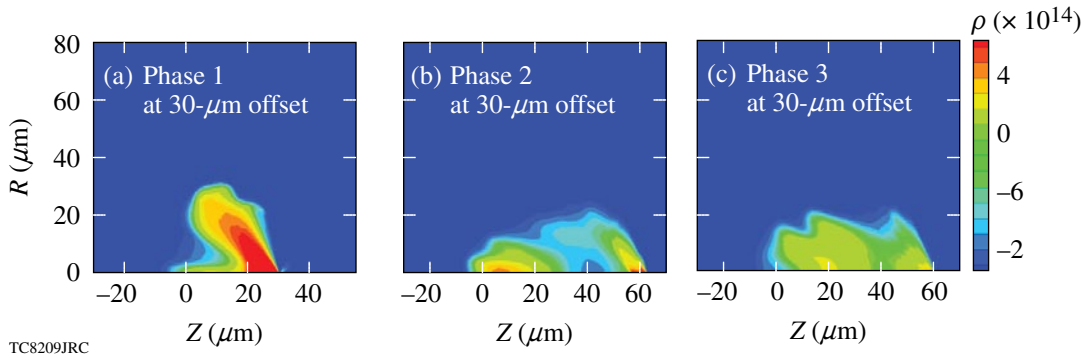
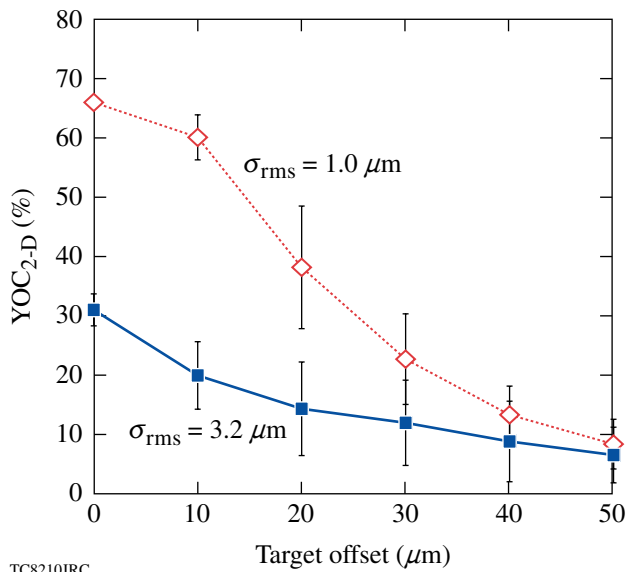


Figure 116.16

The contour plots of $\rho^2 T_i^4$ on the z - r plane, for the corresponding cases [(a), (b), and (c)] in Fig. 116.15. The images indicate where most of the neutrons are probably generated, as the fusion cross section is proportional to $\rho^2 T_i^4$.



TC8210JRC

Figure 116.17

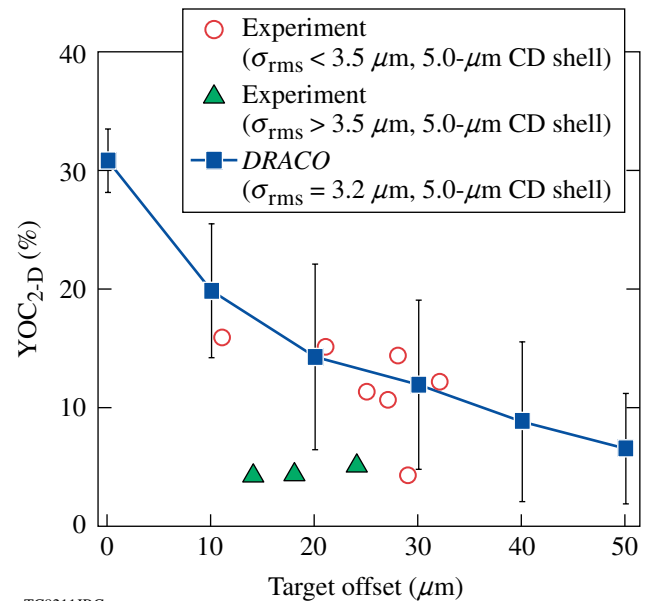
YOC_{2-D} versus target offset for ice roughnesses $\sigma_{\text{rms}} = 1.0 \mu\text{m}$ and $\sigma_{\text{rms}} = 3.2 \mu\text{m}$. The points are obtained by averaging different phases, where the possible YOC_{2-D} range is also marked for each condition.

target offset increases beyond $\sim 10 \mu\text{m}$, the YOC_{2-D} drops more dramatically in the case of $\sigma_{\text{rms}} = 1 \mu\text{m}$ than that of $\sigma_{\text{rms}} = 3.2 \mu\text{m}$. For both cases, the phase-dependent YOC range is significant at a target offset of 20 to 40 μm . When the target offset increases to 50 μm , it becomes the dominant effect and the yield is no longer sensitive to the ice roughness.

4. Comparison to Experiments

In this subsection, we first compare the overall YOC performance as a function of target offset and ice roughness. Secondly, we focus on individual shots by using the actual experimental conditions in our simulations.

The general studies presented in Fig. 116.17 were performed for the case of low-adiabat, thin-CD-shell (5- μm) D₂ implosions. Similar-condition experiments have been conducted on OMEGA.^{15–17} Shots that resulted in a compression of $\langle \rho R \rangle_{\text{exp}} / \langle \rho R \rangle_{1-D} \geq 60\%$ are plotted in comparison with our DRACO simulations ($\sigma_{\text{rms}} = 3.2 \mu\text{m}$) in Fig. 116.18. The shots are divided into two groups according to their target ice roughness, i.e., $\sigma_{\text{rms}} < 3.5 \mu\text{m}$ (circles) and $\sigma_{\text{rms}} > 3.5 \mu\text{m}$ (triangles). We find reasonably good agreement between our DRACO simulation and experiments at an ice-roughness level of $\sigma_{\text{rms}} \sim 3 \mu\text{m}$. Shots with a larger ice roughness ($\sigma_{\text{rms}} > 3.5 \mu\text{m}$) constantly give a lower YOC, which is reasonably below our simulations of $\sigma_{\text{rms}} = 3.2 \mu\text{m}$.



TC8211JRC

Figure 116.18

A comparison of simulated YOC_{2-D} with experimental measurements for low-adiabat ($\alpha \approx 2$ to 3), thin-shell ($\sim 5 \mu\text{m}$) D₂ implosions on OMEGA.

D₂ targets having thick (~10-μm) CD shells were also imploded with the shaped pulse indicated in Fig. 116.19(a). For the thick-shell targets that we studied, the ice layer had a thickness of ~95 μm. The peak laser intensity now increases to ~5 × 10¹⁴ W/cm². In this case, the laser continuously ablates the CD shell during the entire implosion, and there is no ablation transition from CD to D₂. Compared to the thin-shell implosions, the 10-μm-thick-shell targets give a constantly lower YOC ≤ 7%. To understand the yield performance in thick-shell implosions, a general study was also performed through low-ℓ-mode DRACO simulations. The comparison is

made in Fig. 116.19(b). The numerical prediction of YOC_{2-D} from low-ℓ-mode DRACO simulations is higher overall than the experimental measurements by a factor of ~3. In contrast to the thick-shell situation, high-ℓ-mode perturbation growth in thin-shell implosions is probably stabilized when the laser ablation transits into D₂ (high ablation velocity). We speculate that for thick-shell targets, high-mode perturbations such as laser imprinting^{37,38} may become more important since the high-density CD shell stays intact at the ablation surface during the laser irradiation. To that end, we performed simulations to resolve high modes up to ℓ_{max} ≈ 200. The results indicate that a factor of 2 reduction is observed, which brings the high-ℓ-mode simulation results close to experimental measurements for thick-shell implosions.

To get a sense of how YOC degrades when ice roughness increases, we have collected those shots with usual target offsets between ~10 μm and ~40 μm. The results are plotted in Fig. 116.20 and compared with low-ℓ-mode DRACO simulations. For thin-shell (5-μm) targets, our simulations are performed with an average target offset of 25 μm. The numerical results provide an upper limit for these experiments. The overall trend of YOC degradation with increased ice roughness is reasonably well reproduced by DRACO simulations. The 10-μm-thick-shell targets consistently give a lower YOC

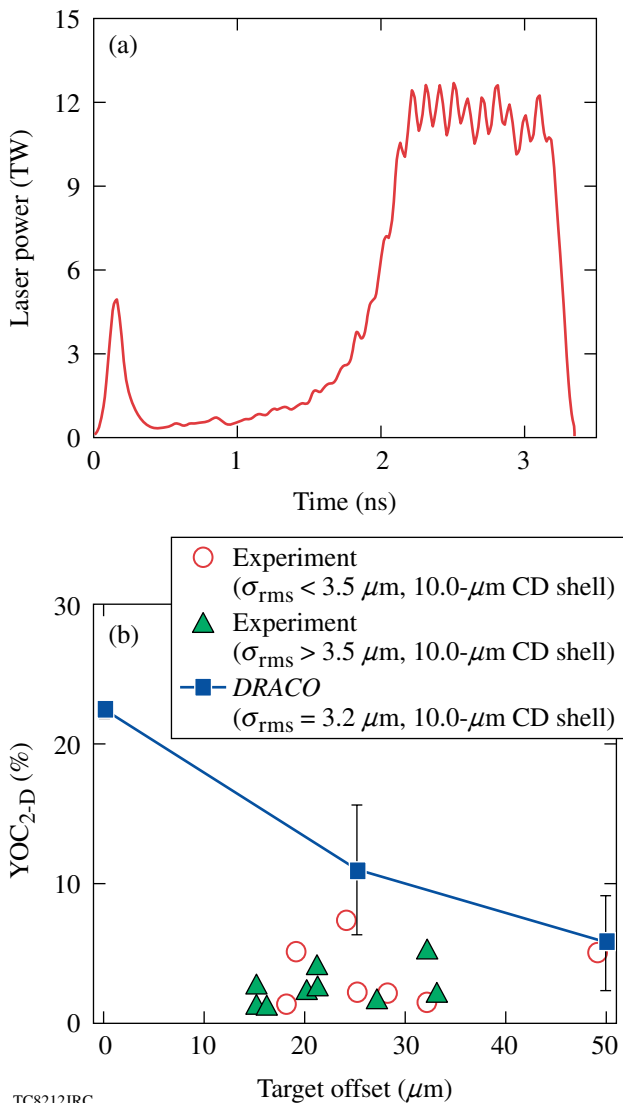


Figure 116.19 (a) A shaped pulse for low-adiabat ($\alpha \approx 2$ to 3), thick-shell (~10-μm) D₂ implosions on OMEGA; (b) low-ℓ-mode DRACO simulated YOC compared with experimental measurements.

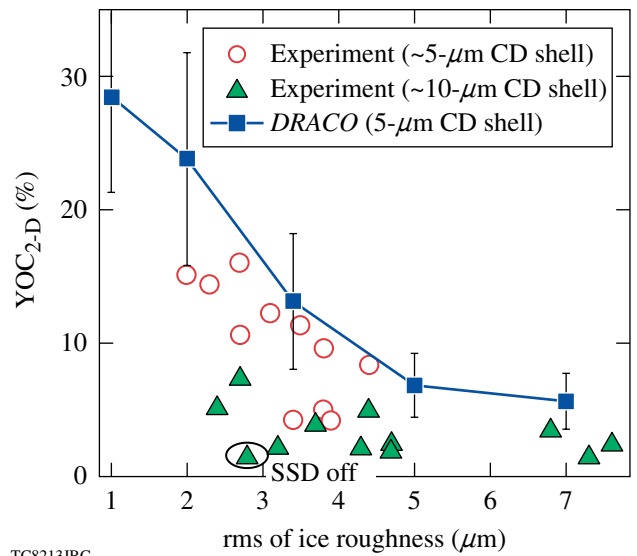


Figure 116.20 The simulated thin-shell YOC_{2-D} as a function of the ice roughness σ_{rms} at a target offset of 25 μm, which is compared to experimental YOC measurements for both 5-μm- and 10-μm-CD-shell implosions at an offset range of 10 to 40 μm. The laser peak intensity (2.5 to 6.0 × 10¹⁴ W/cm²) and pulse shape vary for different experimental shots.

than thin-shell targets. One shot with SSD off is marked in the figure, which shows a very low YOC level.

Finally, we discuss *DRACO* simulations for several individual shots in different conditions. The measured absolute neutron yields, which span two orders of magnitude, are plotted in comparison with *DRACO* simulations in Fig. 116.21. Different low-adiabat pulse shapes are used for these shots with peak intensities varying from 2.5×10^{14} W/cm² to $\sim 6 \times 10^{14}$ W/cm². For most thin-shell (5- μ m) targets, the simulated neutron yields reasonably track the measurements (within a factor of 2). One shot (46864) labeled “shock timing” in Fig. 116.21 has shown a big difference between simulation and experiment. Our constant flux-limiter ($f = 0.06$) simulation gives three-to-four-times-higher neutron yield. For this shot, we noticed that the laser pulse has a higher picket so that the yield and compression performance was sensitive to the thermal transport modeling. Shock timing has played a significant role in target performance. There is also significant discrepancy between the low- ℓ -mode *DRACO* simulation and the experiment for a 10- μ m-thick-shell implosion, which is also labeled in Fig. 116.21. Again, high- ℓ -mode perturbations not included in simulations may have further degraded the neutron yield in experiments.

Besides the total neutron yield, we have also compared the calculated time-resolved neutron rates to those observed in thin-shell experiments. Examples of such comparisons are illustrated in Fig. 116.22. The simulated neutron rate has been

broadened somewhat to account for the time dispersion (due to thermal broadening and/or 3-D effects) in experiments. Good agreement is reached when the Gaussian broadening is done with a width of $\sigma \simeq 100$ ps. We noticed that the thermal broadening contributes only to $\sigma \sim 40$ ps; it is not yet clear about other sources of broadening, although 3-D effect may be the major player. For the low-intensity ($\sim 3 \times 10^{14}$ W/cm²) shot (50267) in which the simulated total yield agrees with the experiment, the measured neutron rate is reproduced by a *DRACO* simulation with a broadening of ~ 100 ps, as shown in Fig. 116.22(a). While, for the mid-intensity ($\sim 6 \times 10^{14}$ W/cm²) shot (49937) illustrated by Fig. 116.22(b), the simulated neutron rate is wider and higher than measurement, the total neutron

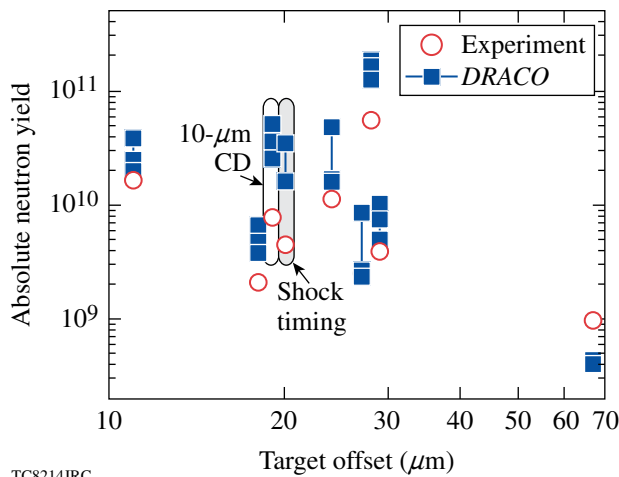


Figure 116.21
The absolute neutron yields are compared between experiments and *DRACO* simulations. Different phases are explored in the simulations. The two shots that are labeled are sensitive to either shock timing or thick-shell implosion for which high- ℓ -mode nonuniformities may be important.

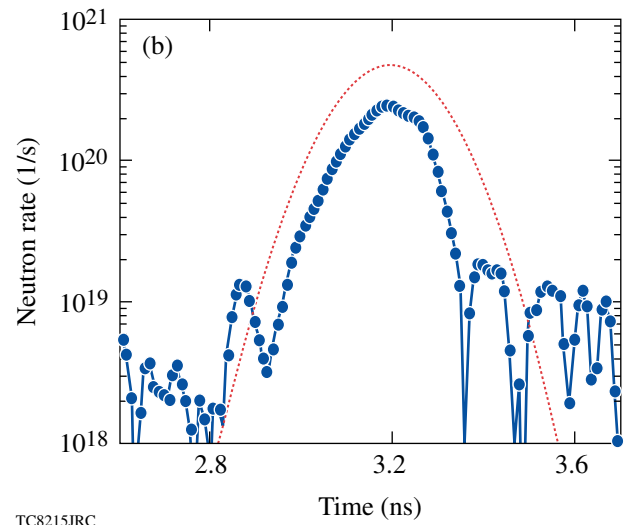
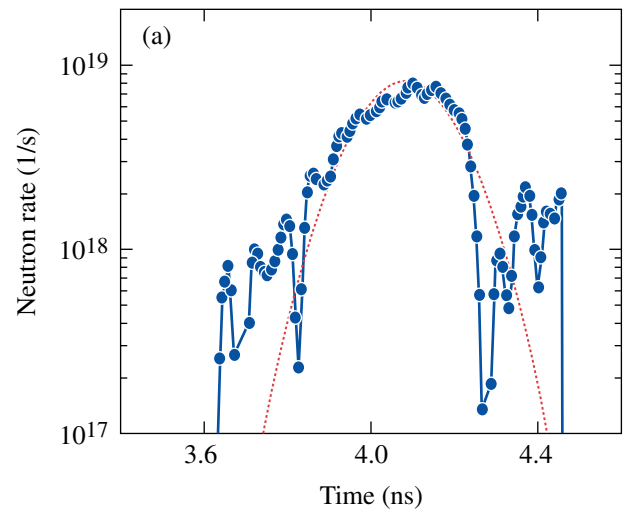


Figure 116.22
The neutron-rate comparison between experiments (circles) and simulations (lines) for (a) low-intensity ($\sim 3 \times 10^{14}$ W/cm²) shot 50267 and (b) mid-intensity ($\sim 6 \times 10^{14}$ W/cm²) shot 49937.

yield in the 2-D simulation is larger than the experimental value by almost a factor of 2. We believe that such a discrepancy may be within the uncertainties that the approximation of a 2-D code may cause in approaching the 3-D reality.

Conclusion

Using 2-D *DRACO* simulations, we have systematically investigated low- ℓ -mode perturbation effects on the neutron-yield degradation of direct-drive, low-adiabat ($\alpha \simeq 2$ to 3) cryogenic D₂ implosions on OMEGA. Despite the limitation of reduced dimensionality, our 2-D simulations show that for thin-shell (5- μ m) targets, the yield degradation can be reasonably explained by the combined perturbations from the target offset, the low- ℓ -mode ice roughness, and low- ℓ -mode laser illumination nonuniformities. In terms of YOC, thick-shell targets generally do not perform as well as thin-shell targets using similar pulse shapes. We show that high- ℓ -mode perturbations such as laser imprinting may play a role in further reducing neutron yields in thick-shell cryogenic implosions. Besides the total neutron yield, the broadened neutron rates from 2-D simulations are also reasonably comparable to measurements, especially for low-intensity and thin-shell implosions. It should also be important to directly carry out such studies for DT implosions because extrapolating these D₂ results to the DT case is not straightforward since shock timing may play a different role. So far fewer DT shots have been conducted on OMEGA than D₂ shots. For these reasons, we leave such a similar investigation of DT implosions for future studies.

ACKNOWLEDGMENT

This work was supported by the U.S. Department of Energy Office of Inertial Confinement Fusion under Cooperative Agreement No. DE-FC52-08NA28302, the University of Rochester, and the New York State Energy Research and Development Authority. The support of DOE does not constitute an endorsement by DOE of the views expressed in this article.

REFERENCES

1. S. Atzeni and J. Meyer-ter-Vehn, *The Physics of Inertial Fusion: Beam Plasma Interaction, Hydrodynamics, Hot Dense Matter*, International Series of Monographs on Physics (Clarendon Press, Oxford, 2004); J. D. Lindl, *Inertial Confinement Fusion: The Quest for Ignition and Energy Gain Using Indirect Drive* (Springer-Verlag, New York, 1998).
2. S. E. Bodner *et al.*, Phys. Plasmas **7**, 2298 (2000).
3. J. D. Lindl, Phys. Plasmas **2**, 3933 (1995).
4. P. W. McKenty, V. N. Goncharov, R. P. J. Town, S. Skupsky, R. Betti, and R. L. McCrory, Phys. Plasmas **8**, 2315 (2001).
5. S. E. Bodner, Phys. Rev. Lett. **33**, 761 (1974); H. Takabe *et al.*, Phys. Fluids **28**, 3676 (1985); H. J. Kull and S. I. Anisimov, Phys. Fluids **29**, 2067 (1986); A. B. Bud'ko and M. A. Liberman, Fluids B **4**, 3499 (1992); V. V. Bychkov, S. M. Goldberg, and M. A. Liberman, Phys. Plasmas **1**, 2976 (1994); J. Sanz, Phys. Rev. Lett. **73**, 2700 (1994); J. G. Wouchuk and A. R. Piriz, Phys. Plasmas **2**, 493 (1995).
6. R. Betti, V. N. Goncharov, R. L. McCrory, P. Sorotokin, and C. P. Verdon, Phys. Plasmas **3**, 2122 (1996); R. Betti, V. N. Goncharov, R. L. McCrory, and C. P. Verdon, Phys. Plasmas **5**, 1446 (1998); V. N. Goncharov, P. McKenty, S. Skupsky, R. Betti, R. L. McCrory, and C. Cherfils-Cl  rouin, Phys. Plasmas **7**, 5118 (2000).
7. B. A. Remington *et al.*, Phys. Rev. Lett. **73**, 545 (1994); K. Shigemori *et al.*, Phys. Rev. Lett. **78**, 250 (1997); S. G. Glendinning, S. N. Dixit, B. A. Hammel, D. H. Kalantar, M. H. Key, J. D. Kilkenny, J. P. Knauer, D. M. Pennington, B. A. Remington, R. J. Wallace, and S. V. Weber, Phys. Rev. Lett. **78**, 3318 (1997); M. M. Marinak *et al.*, Phys. Rev. Lett. **80**, 4426 (1998); C. J. Pawley *et al.*, Phys. Plasmas **6**, 565 (1999).
8. D. L. Tubbs, C. W. Barnes, J. B. Beck, N. M. Hoffman, J. A. Oertel, R. G. Watt, T. Boehly, D. Bradley, P. Jaanimagi, and J. Knauer, Phys. Plasmas **6**, 2095 (1999); C. Cherfils *et al.*, Phys. Rev. Lett. **83**, 5507 (1999).
9. V. A. Smalyuk, T. R. Boehly, D. K. Bradley, V. N. Goncharov, J. A. Delettrez, J. P. Knauer, D. D. Meyerhofer, D. Oron, and D. Shvarts, Phys. Rev. Lett. **81**, 5342 (1998); J. P. Knauer, R. Betti, D. K. Bradley, T. R. Boehly, T. J. B. Collins, V. N. Goncharov, P. W. McKenty, D. D. Meyerhofer, V. A. Smalyuk, C. P. Verdon, S. G. Glendinning, D. H. Kalantar, and R. G. Watt, Phys. Plasmas **7**, 338 (2000); O. Sadot, V. A. Smalyuk, J. A. Delettrez, D. D. Meyerhofer, T. C. Sangster, R. Betti, V. N. Goncharov, and D. Shvarts, Phys. Rev. Lett. **95**, 265001 (2005); H. Azechi *et al.*, Phys. Rev. Lett. **98**, 045002 (2007).
10. F. J. Marshall, R. S. Craxton, J. A. Delettrez, D. H. Edgell, L. M. Elasky, R. Epstein, V. Yu. Glebov, V. N. Goncharov, D. R. Harding, R. Janezic, R. L. Keck, J. D. Kilkenny, J. P. Knauer, S. J. Loucks, L. D. Lund, R. L. McCrory, P. W. McKenty, D. D. Meyerhofer, P. B. Radha, S. P. Regan, T. C. Sangster, W. Seka, V. A. Smalyuk, J. M. Soures, C. Stoeckl, S. Skupsky, J. A. Frenje, C. K. Li, R. D. Petrasso, and F. H. S  guin, Phys. Plasmas **12**, 056302 (2005).
11. P. W. McKenty, T. C. Sangster, M. Alexander, R. Betti, R. S. Craxton, J. A. Delettrez, L. Elasky, R. Epstein, A. Frank, V. Yu. Glebov, V. N. Goncharov, D. R. Harding, S. Jin, J. P. Knauer, R. L. Keck, S. J. Loucks, L. D. Lund, R. L. McCrory, F. J. Marshall, D. D. Meyerhofer, S. P. Regan, P. B. Radha, S. Roberts, W. Seka, S. Skupsky, V. A. Smalyuk, J. M. Soures, K. A. Thorp, M. Wozniak, J. A. Frenje, C. K. Li, R. D. Petrasso, F. H. S  guin, K. A. Fletcher, S. Padalino, C. Freeman, N. Izumi, J. A. Koch, R. A. Lerche, M. J. Moran, T. W. Phillips, G. J. Schmid, and C. Sorce, Phys. Plasmas **11**, 2790 (2004).
12. R. Betti, K. Anderson, J. Knauer, T. J. B. Collins, R. L. McCrory, P. W. McKenty, and S. Skupsky, Phys. Plasmas **12**, 042703 (2005); J. P. Knauer, K. Anderson, R. Betti, T. J. B. Collins, V. N. Goncharov, P. W. McKenty, D. D. Meyerhofer, P. B. Radha, S. P. Regan, T. C. Sangster, V. A. Smalyuk, J. A. Frenje, C. K. Li, R. D. Petrasso, and F. H. S  guin, Phys. Plasmas **12**, 056306 (2005).
13. V. N. Goncharov, J. P. Knauer, P. W. McKenty, P. B. Radha, T. C. Sangster, S. Skupsky, R. Betti, R. L. McCrory, and D. D. Meyerhofer, Phys. Plasmas **10**, 1906 (2003).

14. K. Anderson and R. Betti, *Phys. Plasmas* **10**, 4448 (2003).
15. T. C. Sangster, V. N. Goncharov, P. B. Radha, V. A. Smalyuk, R. Betti, R. S. Craxton, J. A. Delettrez, D. H. Edgell, V. Yu. Glebov, D. R. Harding, D. Jacobs-Perkins, J. P. Knauer, F. J. Marshall, R. L. McCrory, P. W. McKenty, D. D. Meyerhofer, S. P. Regan, W. Seka, R. W. Short, S. Skupsky, J. M. Soures, C. Stoeckl, B. Yaakobi, D. Shvarts, J. A. Frenje, C. K. Li, R. D. Petrasso, and F. H. Séguin, *Phys. Rev. Lett.* **100**, 185006 (2008).
16. V. N. Goncharov, T. C. Sangster, P. B. Radha, R. Betti, T. R. Boehly, T. J. B. Collins, R. S. Craxton, J. A. Delettrez, R. Epstein, V. Yu. Glebov, S. X. Hu, I. V. Igumenshchev, J. P. Knauer, S. J. Loucks, J. A. Marozas, F. J. Marshall, R. L. McCrory, P. W. McKenty, D. D. Meyerhofer, S. P. Regan, W. Seka, S. Skupsky, V. A. Smalyuk, J. M. Soures, C. Stoeckl, D. Shvarts, J. A. Frenje, R. D. Petrasso, C. K. Li, F. Séguin, W. Manheimer, and D. G. Colombant, *Phys. Plasmas* **15**, 056310 (2008).
17. R. L. McCrory, D. D. Meyerhofer, R. Betti, R. S. Craxton, J. A. Delettrez, D. H. Edgell, V. Yu. Glebov, V. N. Goncharov, D. R. Harding, D. W. Jacobs-Perkins, J. P. Knauer, F. J. Marshall, P. W. McKenty, P. B. Radha, S. P. Regan, T. C. Sangster, W. Seka, R. W. Short, S. Skupsky, V. A. Smalyuk, J. M. Soures, C. Stoeckl, B. Yaakobi, D. Shvarts, J. A. Frenje, C. K. Li, R. D. Petrasso, and F. H. Séguin, *Phys. Plasmas* **15**, 055503 (2008).
18. P. B. Radha, T. J. B. Collins, J. A. Delettrez, Y. Elbaz, R. Epstein, V. Yu. Glebov, V. N. Goncharov, R. L. Keck, J. P. Knauer, J. A. Marozas, F. J. Marshall, R. L. McCrory, P. W. McKenty, D. D. Meyerhofer, S. P. Regan, T. C. Sangster, W. Seka, D. Shvarts, S. Skupsky, Y. Srebro, and C. Stoeckl, *Phys. Plasmas* **12**, 056307 (2005); D. Keller, T. J. B. Collins, J. A. Delettrez, P. W. McKenty, P. B. Radha, B. Whitney, and G. A. Moses, *Bull. Am. Phys. Soc.* **44**, 37 (1999).
19. J. A. Marozas, F. J. Marshall, R. S. Craxton, I. V. Igumenshchev, S. Skupsky, M. J. Bonino, T. J. B. Collins, R. Epstein, V. Yu. Glebov, D. Jacobs-Perkins, J. P. Knauer, R. L. McCrory, P. W. McKenty, D. D. Meyerhofer, S. G. Noyes, P. B. Radha, T. C. Sangster, W. Seka, and V. A. Smalyuk, *Phys. Plasmas* **13**, 056311 (2006).
20. B. I. Bennett *et al.*, Los Alamos National Laboratory, Los Alamos, NM, Report LA-7130 (1978).
21. S. X. Hu, V. A. Smalyuk, V. N. Goncharov, J. P. Knauer, P. B. Radha, I. V. Igumenshchev, J. A. Marozas, C. Stoeckl, B. Yaakobi, D. Shvarts, T. C. Sangster, P. W. McKenty, D. D. Meyerhofer, S. Skupsky, and R. L. McCrory, *Phys. Rev. Lett.* **100**, 185003 (2008).
22. R. Cauble *et al.*, *Phys. Rev. Lett.* **80**, 1248 (1998).
23. W. F. Huebner *et al.*, Los Alamos National Laboratory, Los Alamos, NM, Report LA-6760-M (1977).
24. R. C. Malone, R. L. McCrory, and R. L. Morse, *Phys. Rev. Lett.* **34**, 721 (1975).
25. S. P. Regan, R. Epstein, V. N. Goncharov, I. V. Igumenshchev, D. Li, P. B. Radha, H. Sawada, W. Seka, T. R. Boehly, J. A. Delettrez, O. V. Gotchev, J. P. Knauer, J. A. Marozas, F. J. Marshall, R. L. McCrory, P. W. McKenty, D. D. Meyerhofer, T. C. Sangster, D. Shvarts, S. Skupsky, V. A. Smalyuk, B. Yaakobi, and R. C. Mancini, *Phys. Plasmas* **14**, 056305 (2007).
26. T. R. Boehly, E. Vianello, J. E. Miller, R. S. Craxton, T. J. B. Collins, V. N. Goncharov, I. V. Igumenshchev, D. D. Meyerhofer, D. G. Hicks, P. M. Celliers, and G. W. Collins, *Phys. Plasmas* **13**, 056303 (2006).
27. A. Sunahara, J. A. Delettrez, C. Stoeckl, R. W. Short, and S. Skupsky, *Phys. Rev. Lett.* **91**, 095003 (2003).
28. J. Delettrez, *Can. J. Phys.* **64**, 932 (1986); J. Delettrez, R. Epstein, M. C. Richardson, P. A. Jaanimagi, and B. L. Henke, *Phys. Rev. A* **36**, 3926 (1987).
29. V. A. Smalyuk, S. X. Hu, V. N. Goncharov, D. D. Meyerhofer, T. C. Sangster, D. Shvarts, C. Stoeckl, B. Yaakobi, J. A. Frenje, and R. D. Petrasso, *Phys. Rev. Lett.* **101**, 025002 (2008); V. A. Smalyuk, S. X. Hu, V. N. Goncharov, D. D. Meyerhofer, T. C. Sangster, C. Stoeckl, and B. Yaakobi, *Phys. Plasmas* **15**, 082703 (2008).
30. T. R. Boehly, D. L. Brown, R. S. Craxton, R. L. Keck, J. P. Knauer, J. H. Kelly, T. J. Kessler, S. A. Kumpan, S. J. Loucks, S. A. Letzring, F. J. Marshall, R. L. McCrory, S. F. B. Morse, W. Seka, J. M. Soures, and C. P. Verdon, *Opt. Commun.* **133**, 495 (1997).
31. Y. Lin, T. J. Kessler, and G. N. Lawrence, *Opt. Lett.* **20**, 764 (1995).
32. T. R. Boehly, V. A. Smalyuk, D. D. Meyerhofer, J. P. Knauer, D. K. Bradley, R. S. Craxton, M. J. Guardalben, S. Skupsky, and T. J. Kessler, *J. Appl. Phys.* **85**, 3444 (1999).
33. S. Skupsky, R. W. Short, T. Kessler, R. S. Craxton, S. Letzring, and J. M. Soures, *J. Appl. Phys.* **66**, 3456 (1989); J. E. Rothenberg, *J. Opt. Soc. Am. B* **14**, 1664 (1997); S. P. Regan, J. A. Marozas, J. H. Kelly, T. R. Boehly, W. R. Donaldson, P. A. Jaanimagi, R. L. Keck, T. J. Kessler, D. D. Meyerhofer, W. Seka, S. Skupsky, and V. A. Smalyuk, *J. Opt. Soc. Am. B* **17**, 1483 (2000).
34. D. H. Edgell, W. Seka, R. S. Craxton, L. M. Elasky, D. R. Harding, R. L. Keck, and M. D. Wittman, *Fusion Sci. Technol.* **49**, 616 (2006).
35. T. C. Sangster, R. Betti, R. S. Craxton, J. A. Delettrez, D. H. Edgell, L. M. Elasky, V. Yu. Glebov, V. N. Goncharov, D. R. Harding, D. Jacobs-Perkins, R. Janezic, R. L. Keck, J. P. Knauer, S. J. Loucks, L. D. Lund, F. J. Marshall, R. L. McCrory, P. W. McKenty, D. D. Meyerhofer, P. B. Radha, S. P. Regan, W. Seka, W. T. Shmayda, S. Skupsky, V. A. Smalyuk, J. M. Soures, C. Stoeckl, B. Yaakobi, J. A. Frenje, C. K. Li, R. D. Petrasso, F. H. Séguin, J. D. Moody, J. A. Atherton, B. D. MacGowan, J. D. Kilkenny, T. P. Bernat, and D. S. Montgomery, *Phys. Plasmas* **14**, 058101 (2007).

36. V. A. Smalyuk, D. Shvarts, R. Betti, J. A. Delettrez, D. H. Edgell, V. Yu. Glebov, V. N. Goncharov, R. L. McCrory, D. D. Meyerhofer, P. B. Radha, S. P. Regan, T. C. Sangster, W. Seka, S. Skupsky, C. Stoeckl, B. Yaakobi, J. A. Frenje, C. K. Li, R. D. Petrasso, and F. H. Séguin, *Phys. Rev. Lett.* **100**, 185005 (2008).
37. D. H. Kalantar, M. H. Key, L. B. Da Silva, S. G. Glendinning, B. A. Remington, J. E. Rothenberg, F. Weber, S. V. Weber, E. Wolfrum, N. S. Kim, D. Neely, J. Zhang, J. S. Wark, A. Demir, J. Lin, R. Smith, G. J. Tallents, C. L. S. Lewis, A. MacPhee, J. Warwick, and J. P. Knauer, *Phys. Plasmas* **4**, 1985 (1997); M. Nakai *et al.*, *Phys. Plasmas* **9**, 1734 (2002); V. A. Smalyuk, O. Sadot, J. A. Delettrez, D. D. Meyerhofer, S. P. Regan, and T. C. Sangster, *Phys. Rev. Lett.* **95**, 215001 (2005); V. A. Smalyuk, V. N. Goncharov, K. S. Anderson, R. Betti, R. S. Craxton, J. A. Delettrez, D. D. Meyerhofer, S. P. Regan, and T. C. Sangster, *Phys. Plasmas* **14**, 032702 (2007).
38. R. J. Taylor, A. L. Velikovich, J. P. Dahlburg, and J. H. Gardner, *Phys. Rev. Lett.* **79**, 1861 (1997); A. L. Velikovich *et al.*, *Phys. Plasmas* **5**, 1491 (1998); V. N. Goncharov, S. Skupsky, T. R. Boehly, J. P. Knauer, P. McKenty, V. A. Smalyuk, R. P. J. Town, O. V. Gotchev, R. Betti, and D. D. Meyerhofer, *Phys. Plasmas* **7**, 2062 (2000); P. B. Radha, V. N. Goncharov, T. J. B. Collins, J. A. Delettrez, Y. Elbaz, V. Yu. Glebov, R. L. Keck, D. E. Keller, J. P. Knauer, J. A. Marozas, F. J. Marshall, P. W. McKenty, D. D. Meyerhofer, S. P. Regan, T. C. Sangster, D. Shvarts, S. Skupsky, Y. Srebro, R. P. J. Town, and C. Stoeckl, *Phys. Plasmas* **12**, 032702 (2005).